THE JOURNAL OF PHYSICAL CHEMISTRY C

Article

pubs.acs.org/JPCC

Effects of Nanoscale Heterogeneities on the Reactivity of Shocked Erythritol Tetranitrate

David Furman,[†,‡] Ronnie Kosloff,[†] and Yehuda Zeiri*[,‡,§]

[†]Fritz Haber Research Center for Molecular Dynamics, Institute of Chemistry, Hebrew University of Jerusalem, Jerusalem 91904, Israel

[‡]Division of Chemistry, Nuclear Research Center Negev, P.O. Box 9001, Beer-Sheva 84190, Israel

[§]Department of Biomedical Engineering, Ben Gurion University, Beer-Sheva 94105, Israel

ABSTRACT: The mechanochemical effects of 5 nm spherical heterogeneities on the reactivity of shocked crystalline erythritol tetranitrate (ETN), an emerging improvised explosive, are revealed for the first time. Reactive molecular dynamics simulations in conjunction with the symmetric plate-impact technique, are employed to characterize different stages of the process, including shock–void interaction, void collapse, enhanced reactivity, and subsequent molecular decomposition. The formation of supersonic nanojets from the proximal void surface is observed to greatly enhance local heating following impact of the nanojets on the distant void surface. It is demonstrated that the nanovoid collapse closely matches a Rayleigh-type hydrodynamic bubble collapse, including a spherical-to-crescent shape transformation. The chemical decomposition mechanism of condensed phase ETN is analyzed and is shown to follow a unimolecular path. The molecular decomposition of a defect containing crystal occurs with significantly higher rates compared to the perfect crystal.

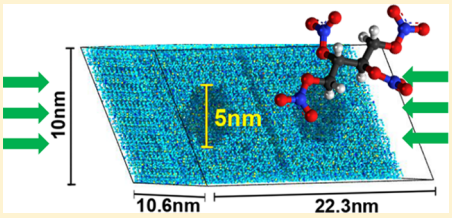

INTRODUCTION

Nanotechnology has revolutionized the traditional paradigm of materials science and engineering, enabling the manipulation of the building blocks of matter.[1−5] At these ever-smaller dimensions, mechanochemical effects may become predominantly responsible for unique material responses toward external stimuli.[6−8] In the following, we examine the effects of 5 nm diameter spherical voids on the shock induced decomposition of an otherwise perfect, single crystal of erythritol tetranitrate (ETN). Although it was first synthesized in 1849, little is known about its decomposition mechanism and response to shock loading. Recently, ETN has grown in popularity as a "homemade" explosive due to the increasing public demand and subsequent large scale industrial production of its precursor, erythritol, used as a sweetener.[9] The development processes of efficient chemical probes and taggants for "sniffing" of materials rely heavily on the detailed chemical mechanisms, intermediates, and stable decomposition products in the decomposition sequence of the explosive. Since analytical methods still lack the necessary resolution for on-the-fly analysis of the initiation pathways in condensed phase explosives, atomistic simulations with femtosecond resolution are a prime alternative.

Numerous computational studies have been carried out over the past years to study the response of solid energetic materials to impact, heating, and acoustic or electromagnetic stimuli. However, many of these used an idealized representation of the material, where the microstructural heterogeneities were ignored, i.e., simulating a perfect single crystal.[10−14] Conventional and improvised explosives, in particular, are characterized with heterogeneities such as crystal defects, grain boundaries, inclusions, solvent residues, and crystal–binder interfaces that may serve as sinks for external mechanical energy. It is generally accepted that local defect sites in the material can serve as energy localization sites (hot spots) and thus are an essential step for a reaction runaway to occur, overcoming heat dissipation channels so to sustain a stable detonation wave in the material. Indeed, several different such initiation mechanisms have been proposed over the years, including pore collapse, shear, viscoplastic heating, work on trapped gases, and Mach stems. Calculations suggested that collapsing pores are the most effective mechanism.[15] Localized material heterogeneities could form during synthesis procedures (i.e., incorporating impurities, dislocations) or during more advanced material processing stages (i.e., forming cracks, crystal–binder grain boundaries). Unfortunately, since the pioneering works of Bobolev,[16] not much progress has been made in understanding the role of submicrometer and nanoscale material heterogeneities from the experimental point of view. The main reason is that most experimental studies have concentrated on the effects of micrometer-scale[17−19] and millimeter-scale[20] voids, since these are much easier to incorporate and monitor in a controlled fashion using conventional optical methods. Moreover, the spatial distribution of the voids is rarely known; thus a statistical interpretation is usually sought.[21] Thus, computer modeling and molecular dynamics simulations play a pivotal role in the understanding of hot spot initiation and related mechanochemical phenomena.[22−30] While there is no universal agreement on the optimal

Received: November 16, 2016
Published: November 21, 2016

DOI: 10.1021/acs.jpcc.6b11543
J. Phys. Chem. C 2016, 120, 28886−28893

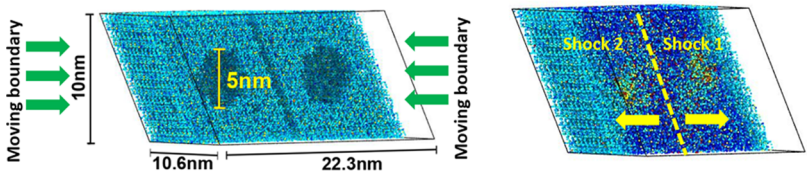

Figure 1. (left) Cut-plane view of the initial equilibrated state. The system is composed of two identical slabs of material 2 Å apart from each other. In each slab, all the molecules residing within a sphere of a defined diameter (5 nm) are removed to form a nanoscale spherical void and the symmetric plate impact methodology is carried out. (right) Cut-plane view of the system a few picoseconds after the two identical slabs collided and generated two oppositely propagating shock waves. Atoms are colored by the magnitude of their velocity, and shock propagation is in the [100] direction.

void size that leads to detonation for a given impact load, it is generally assumed that void size should be in the range ~100 nm to a few micrometers.[17,18] On the other hand, it has been speculated that ultrasmall voids do not produce high enough temperatures during and after collapse; hence, eventually they cool down and quench without influencing the material decomposition rate. Recent USAXS measurements[31,32] on TATB-based explosives have identified a bimodal pore distribution centered on 10 nm and a wider peak extending from 50 nm to 2 μm. The nanoscale voids were attributed to defects within the crystallites, while the larger voids were assigned to voids between grains or grain−binder interfaces.

The passage of a shock wave inside a unit cell of a material is an ultrafast process compared to the time scale associated with the formation of secondary intermediates and final products. As a result, most of the computational studies reporting on shock induced initiation of condensed phase energetic materials were limited to the short duration of the shock passage via the studied system.[14,33,34] This severe time restriction prohibited the shocked system from reaching its chemical steady state, due to shock reflection at the computational cell boundaries. Hence, the chemical transformations occurring after the shock wave passage were not considered. Consequently, any mechanism that leads to delayed heating and subsequent decomposition was disregarded. To overcome this time scale limitation in the study of long-time chemical effects of nanovoids under shock loading, ReaxFF simulations were conducted in conjunction with the symmetric plate impact methodology[35,36] (Figure 1). This method allows us to study the reactive events occurring in the Chapman−Jouguet state for durations up to ~10 ns, as long as the integration error is negligible and energy conservation is satisfied. Typical reaction zone widths of several perfect single crystals and plastic bonded explosives range from 10 to 400 ns in duration.[37] In the present study, the longest simulation duration is 17.5 ps, an order of magnitude smaller than experimental reaction zone widths; thus it is a compromise between simulation time and steady state kinetics.

SYMMETRIC PLATE IMPACT SIMULATION METHODOLOGY

Two different systems were prepared for subsequent symmetric plate impact simulation. System 1 is a perfect, single crystal of ETN, composed of 209 664 atoms (8064 molecules) with dimensions 201.6 × 16.4 × 27.8 Å. The system is divided and separated into two identical slabs of material which collide at a desired impact velocity, simulating a symmetric plate impact experiment. System 2 is the defected crystal system where a spherical void of 5 nm diameter was introduced in each one of the two slabs by removing the molecules inside the void. Simulations used a time step of 0.1 fs and employed three-dimensional (3D) periodic boundary conditions. Although the force field chosen for this study was previously successfully used to predict the decomposition chemistry of pentaerythritol tetranitrate (PETN) in numerous studies,[12,14,38] we validated the force field to accurately reproduce density functional theory (DFT) calculations of major unimolecular decomposition channels of ETN, as shall be discussed in the text.

All systems were initially energy minimized using a standard conjugate gradient procedure. Equilibration steps for the temperature (*NVT* ensemble) and pressure (*NPT* ensemble) were carried out on the minimized systems using a Berendsen thermostat and barostat, respectively. Temperature was kept at 200 K and pressure was kept at 1 atm with coupling constants of 50 and 500 fs, respectively. Equilibration simulations lasted up to 10 ps so as to relax the initial thermodynamic state of the systems.

The equilibrated systems (200 K and 1 atm) were subjected to a three-stage symmetric plate-impact simulation strategy (Figure 2). This approach was previously used mainly in studies

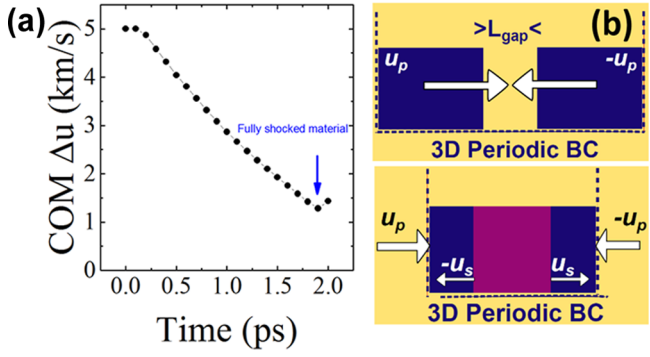

Figure 2. (a) Center of mass velocity difference between the two identical material slabs (km/s). (b) Schematic representation of the simulation protocol. Top figure is the initial state of the system where two identical but opposite velocities, u_p, are given to the two identical slabs separated by a distance L_{gap}. Bottom figure shows the collision and the resultant shock waves moving toward the boundaries at velocities u_s.

of shock wave propagation in metals and metal composites.[35,39] Shock loading is simulated by the addition of an external particle velocity, v_p = 2.5 km/s in the present study, to each atom in the left part of the material and a velocity, $-v_p$, to the atoms in the right slab. This impact velocity is slightly above the longitudinal speed of sound in PETN, a very similar nitrate ester in terms of chemical composition, structure, and performance. To avoid material tension, both positions of the left and right periodic boundaries of the computational cell were dynamically adjusted according to $l_{(x)} = l_0 - v_p t$. Following

DOI: 10.1021/acs.jpcc.6b11543
J. Phys. Chem. C 2016, 120, 28886−28893

the collision between the slabs, two identical shock waves are formed that propagate from the interface to the outward direction in each slab. Once the two shock waves reach the two opposite boundaries, the system corresponds to a singly, fully shocked state. The instant in time where the two shock waves arrive at the boundaries can be precisely determined from the difference in the center of mass particle velocity across opposite slabs.[35,36] Once this stage is reached, the moving boundaries are fixed and the system is allowed to evolve as a function of time. This stage allows tracking shock-induced chemical transformations which are decoupled from the time scale of shock propagation and can be studied for much longer durations compared with shock duration.

RESULTS

I. Density Map for Shock-Induced Decomposition. The two-dimensional (2D) density profiles of the perfect and defected systems are presented in Figure 3. It is clearly seen

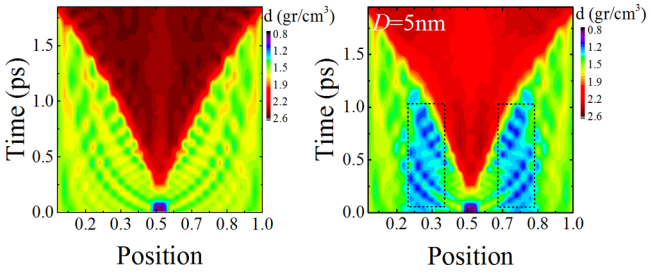

Figure 3. Density evolution during shock initiation of ETN with a particle velocity of 2.5 km/s. (left) Single crystal ETN. (right) ETN with a nanovoid of 5 nm diameter. Black dots mark the position of the nanovoids in both slabs of material. Note that the position axis is a a unitless fractional scale in all figures, such that 0.0 is the position of the left boundary and 1.0 is the position of the right boundary of the combined slabs, in the longitudinal direction. The lowest density values belong to the initial void between two material slabs and the spherical nanovoid.

that the shock wave propagation induces a fringelike pattern in both systems. The initial impact at the collision between the two identical slabs generates high density states along the longitudinal direction. The propagation velocity of the shock wave can be evaluated from the shock front position divided by the respective time window. The calculated shock wave velocity is nearly 6.7 km/s for a particle velocity of 2.5 km/s. This value is smaller by 0.7 km/s compared to the detonation velocity at the CJ state (7.4 km/s at d = 1.54 g/cm^3). During the passage of the shock wave through the system, the thermodynamic state is still far from equilibrium. This is verified by the product species evolution (Figure 7). The final density reached in the fully shocked state is about 2.4 g/cm^3. The presence of the nanovoids results in drastic effects on the density variation during the shock wave propagation in the material. The presence of the nanovoids leads to formation of local low density pockets, thus forming a low impedance interface, where the upstream material is ejected into it in the form of a supersonic nanojet. The nanojets propagate at higher velocities to a greater extent than the rest of the material, with observed velocities of up to 5 km/s, being twice the initial particle velocity. Moreover, starting at t = 1 ps, the shock front accelerates, as can be seen from its bending as time progresses (Figure 3). This acceleration originates from the interaction of the incident shock wave with the nanovoid having a significantly lower acoustic impedance, hence leading to a divergent shock−void geometry and shock focusing.[40] The void collapse dynamics are further analyzed and discussed below (Figure 9). The formation of the supersonic molecular jets together with the increased rate of collapse supports the increase in shock wave velocity. This behavior is not seen in the case of a single crystal ETN, where the propagation velocity of the shock front remains largely stable. The lower average density observed in Figure 4 for the nanovoid containing slabs

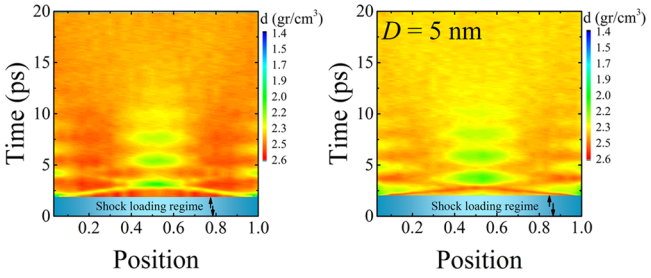

Figure 4. Late time density evolution following shock initiation of ETN with a particle velocity of 2.5 km/s. (left) Single crystal ETN. (right) ETN with a nanovoid of 5 nm diameter.

is related to the decreased amount of material in the initial slabs used. The density reached following the shock loading in both systems is approximately 2.4−2.6 g/cm^3. Some oscillations are evident in Figure 4 originating from the newly formed, highly energetic, intermediate radicals at the plane of impact between the two slabs. When local thermal equilibrium is reached at t = 10 ps (Figure 6), the oscillations disappear.

II. Temperature Map for Shock-Induced Decomposition. The impact and resulting shock wave generate immense heating of the downstream material. While the upstream material temperature is 200 K, the molecules near the impact interface reach temperatures above 2000 K. During the shock loading process that lasts here 1.5−2 ps, the heat wave is generated mainly by pressure−volume work done on the material, since the main chemical events occurring during this process are endothermic (Figure 7). Comparing the two temperature maps for the perfect single crystal and the defected system clearly shows a drastic increase in the heated zone due to the nanovoid during the shock wave passage inside the system (Figure 5). Inside the voids, the average temperature reaches 1700 K while the surrounding temperatures are in the range 1200−1600 K. In contrast, in the case of a perfect crystal, an intermediate temperature of 950 K is obtained throughout the system except at the impact interface. The higher

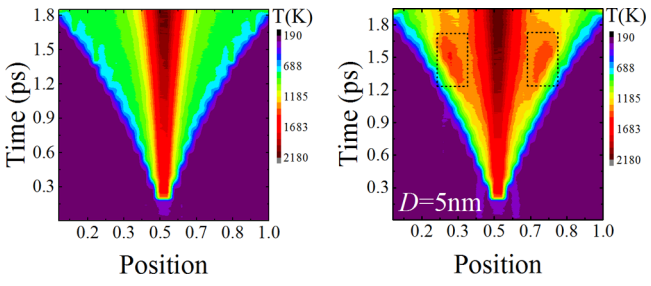

Figure 5. Temperature evolution during shock initiation of ETN. (left) Single crystal ETN. (right) ETN with a nanovoid of 5 nm diameter. Black dots mark the position of the nanovoid in both parts of material.

DOI: 10.1021/acs.jpcc.6b11543
J. Phys. Chem. C 2016, 120, 28886−28893

temperatures of the defected system accelerate material thermal decomposition processes and the formation of intermediate radicals, such as NO_2 and NO observed in Figure 7. Similar dramatic heating effects due to nanoscale bubbles in liquids were shown in recent studies of nanobubble collapse in liquids.[41] The initial enhanced heating leads to a faster temperature rise toward the final temperature as can be observed from the late time temperature evolution in Figure 6.

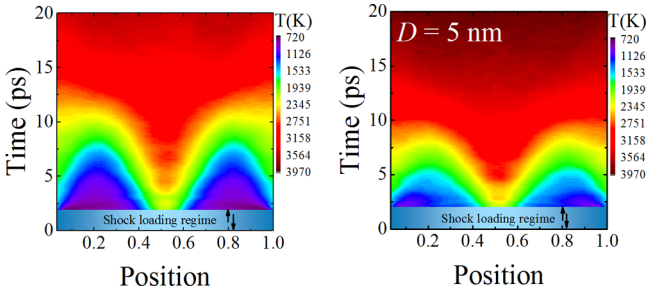

Figure 6. Late-time temperature evolution following shock initiation of ETN. (left) Single crystal ETN. (right) ETN with a nanovoid of 5 nm diameter.

The final temperature reached in the defected system reaches nearly 4000 K, which is almost 500 K higher than in the perfect system. Hence, the evolution of intermediate decomposition products proceeds at much higher rates, as is shown in Figure 7. Moreover, despite the small cavity diameter, the nanovoid collapse follows closely the collapse dynamics of much larger micrometer size bubbles in liquids; see Figure 9.

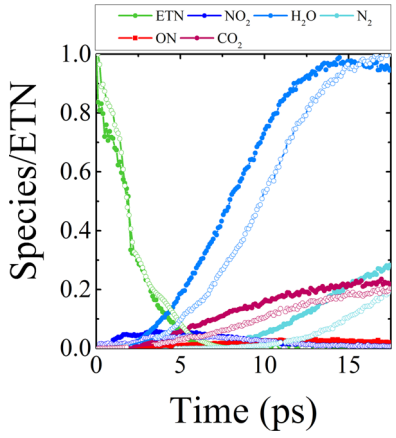

Figure 7. Evolution of reactive events during shock initiation of ETN with particle velocity of 2.5 km/s. Filled circles refer to the case of defected single crystal, and empty circles refer to perfect single crystal. Representative radical intermediate decomposition species are also shown, while transient, covalent ETN−ETN dimers have been omitted for clarity.

III. Reactive Events during and after Shock Loading.

The initial chemical events that take place during the passage of the shock wave and at later times are presented in Figure 7.

After a short induction period of roughly 0.25 ps in the case of a perfect single crystal, decomposition begins with the unimolecular homolytic cleavage of the $O-NO_2$ bond in parent ETN molecules. The calculated bond energies predicted by ReaxFF, 29 and 33 kcal/mol, are in good agreement with the DFT values of 26.1 and 29.0 kcal/mol for the internal and external $O-NO_2$ groups, respectively. Since this route has the lowest energy barrier among several possible unimolecular decomposition channels, NO_2 radicals are produced and their amount steadily increases during shock loading. Remarkably, the decomposition of ETN proceeds much faster in the defected system. For example, by the time of t = 0.7 ps, only 20% of ETN was decomposed in the perfect system, while 30% decomposition was reached in the defected system. This trend closely matches the more significant production of NO_2 radicals in the defected system at initial times. The formation of NO radicals is depressed in the perfect system, while in the defected system a relative enhancement in NO production is seen. Interestingly, no NO_3 radicals are obtained in either system, indicating that the competing nitro−nitrite isomerization reaction, commonly responsible for the appearance of NO, is suppressed under the conditions of shock loading at v_p = 2.5 km/s. In addition to the effect on the early decomposition events, the presence of the nanovoids affects the long-time evolution of the decomposition process. In the case of the defected system, the appearance of stable gaseous species, such as H_2O and N_2, becomes noticeable much earlier than in the perfect system. For example, the formation of H_2O in the perfect crystal system lags behind by approximately 1.75 ps compared to the defected system. It is noteworthy to stress that the enhancement of secondary intermediates and stable products, i.e., "late chemistry", would not be noticed in ordinary nonequilibrium shock loading simulations due to the time limitation imposed by the small computational cell compared to the shock velocity. Thus, very large computational cells and as a result prohibitively expensive computational resources would be needed to observe such effects.[34] The major carbon-containing product observed in the simulations is CO_2 for both systems. This is because ETN, a secondary nitrate ester, has a slightly positive oxygen balance.[42] Since there are no experimental measurements or theoretical predictions of the shock initiation of ETN that we are aware of, it is of interest to compare the chemistry obtained in our simulations to previous shock initiation simulations of PETN.[14]

In the paper by Budzien et al., two particle velocities (3 and 4 km/s) were simulated by the ramming of a PETN perfect single crystal toward a repulsive wall.[14] It was found that the main difference between the two shock velocities was the time required to reach the same qualitative behavior. Hence, the secondary and final gaseous products were produced much faster in the strongly shocked system. Similarly, this effect manifests itself in our simulations, where the presence of the nanovoid induces substantial local heating. In turn, this develops a "time gap" between the species evolution when comparing the perfect and defected systems. Additionally, it was found that the main initiation reaction under both impact speeds was the cleavage of $O-NO_2$ bond,[18] as is also found in our simulations. This should not be surprising, since both ETN and PETN show very similar detonation properties as were recently measured.[43] The results related to the production of detonation products can be compared to estimations based on equilibrium codes such as Cheetah, although with great caution. Experimentally, the product distributions are known to depend on the temperature[44] and loading conditions.[45] Therefore, different experimental methods might differ in their estimation of relative amounts of decomposition products. Moreover, our results correspond to the compressed CJ state, while experimental measurements typically sample from isentropically expanded and cooled systems. According to Cheetah

DOI: 10.1021/acs.jpcc.6b11543
J. Phys. Chem. C 2016, 120, 28886−28893

calculations,[43] the major decomposition products and their molar ratios for ETN are H_2O (0.31), CO_2 (0.41), and N_2 (0.17). Although thermochemical product distributions are the outcome of a full chemical equilibrium state reached by the products, it is still possible to qualitatively compare the product distributions to the quasi-steady-state distributions obtained in our simulations. The mole fractions obtained here are H_2O (0.58), CO_2 (0.14), and N_2 (0.27). The differences observed in these values are due to the aforementioned reasons. It is known that further expanding the detonation products in variable-volume simulations usually leads to much better agreement with thermochemical estimates.[14] It is also possible to compare the ratio between the amounts of a product species relative to the initial number of ETN molecules. The asymptotic relative amounts of the decomposition products obtained in our simulations, H_2O (1.1), CO_2 (0.25), and N_2 (0.44), match closely to those reported for shock loaded PETN:[14] H_2O (1.1 ± 0.2), CO_2 (0.20 ± 0.2), and N_2 (0.23 ± 0.2).

IV. Atomistic Dynamics of a Nanovoid Collapse. To obtain insight into the nanovoid collapse dynamics, the process is analyzed in terms of the displacement vectors of each atom in the system. Figure 8 presents snapshots of particle position displacements at different times. The snapshots are of a 15 Å wide slice along the computational cell, starting with the initial system and ending with the final collapse of the nanovoids at t = 1.45 ps after impact. The green vectors attached to each atom near the nanovoid boundary are proportional to the displacement of the atom relative to its position in the initial state. Each atom is also colored by the magnitude of its displacement, so at t = 0 ps where every atom is at its initial position, no net motion occurs. Once the two slabs collide and the shock waves reach the nanovoids, ejection of molecules into the void is observed and represented by the large displacement vectors. The fastest molecules reach velocities of up to 5 km/s. In the final stage of the collapse process at t = 1.45 ps, the two nanovoids are compressed with hot gaseous species mainly composed of NO_2 and the remaining fragment from ETN after homolytic bond cleavage (ETN-NO_2). The normalized variation of nanovoid average diameter at different instances during the collapse process is presented in Figure 9 (see details below). It is clearly seen that after about 0.8 ps the nanovoids are no longer spherical; in fact, their spherical shape becomes sheared when the shock hits the proximal void surface at approximately t = 0.6 ps, and a crescentlike shape is obtained.

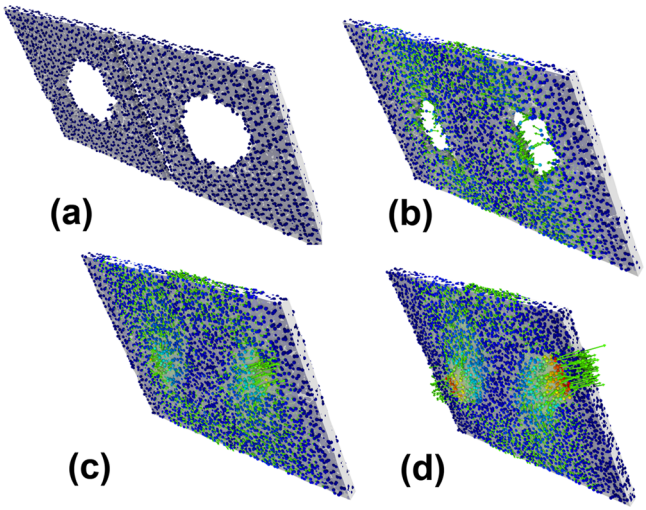

Figure 8. Time snapshots of a thin slice (10 Å) of the two colliding ETN parts. Atoms are colored by the net atomic displacement realtive to the initial state (t = 0 ps). Green arrrows are used for the visualization of the net displacement, and a surface reconstruction was used to better visualize the void collapse dynamics. (a) t = 0 ps, (b) t = 0.8 ps, (c) t = 1.4 ps, and (d) t = 1.6 ps.

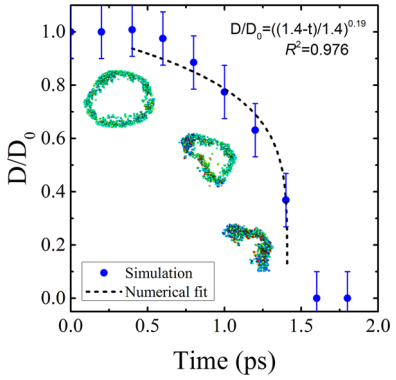

Figure 9. Change in effective diameter of the nanovoid as a function of time during the passage of the shock wave. Error bars represent the uncertainty in determining the effective length based on the image processing method. Results were fitted to a power law with resemblence to the Rayleigh collapse of a bubble in a liquid.

It is of interest to compare the dynamics of the 5 nm void collapse with that of macroscopic pores to examine if there is any size effect associated with the shock–void interaction and in the detonation chemistry. In a recent study of a single pore collapse using continuum scale simulations,[46] pores of diameters in the range 0.05–1 μm were introduced into an otherwise homogeneous 1,3,5-triamino-2,4,6-trinitrobenzene (TATB) 2D slab for several input shock pressures (10–36 GPa). It was found that the proximal pore surface jets across and closes the pore around twice the speed of the shock front. A similar phenomenon was observed in our simulations, where the molecular jets traveled up to 5 km/s, which is twice the particle velocity. In addition, it was revealed that the collapse process is not spherically symmetric but is of a toroidal shape much like that observed for the 5 nm diameter voids in the present simulations. Interestingly, from the analysis of burning front velocities, it was shown that small pores (on the order of 50 nm) can in fact burn a significant amount of material before stagnation for higher shock pressures (24–36 GPa). In comparison, for the 2.5 km/s particle velocity and 5 nm diameter void case, in the present simulations, the pressure reaches a value of 24 GPa. This demonstrates the importance of nanoscale voids in the material. Finally, it is worth noting that isolated nanoscale voids might be subcritical in the sense that at some point they shall self-extinguish due to heat losses by conduction to surrounding material; however, taking into account the spatial distribution of material defects raises the possibility of void–void coalescence which can lead to significant material burnup and subsequent detonation.

To obtain a quantitative measure of the collapse dynamics, the nanovoid effective diameter was calculated in the following manner. The inner area of the void was measured using image analysis techniques, and an effective diameter was estimated based on the formula for a circle. This method is more accurate than other methods used in the literature, such as evaluation of the diameter using a few representative line segments across the

DOI: 10.1021/acs.jpcc.6b11543
J. Phys. Chem. C 2016, 120, 28886–28893

void from the circumference and calculating the average line length.[47] To quantitatively characterize the collapse dynamics, a numerical fitting procedure was performed for the calculated series of void diameters as a function of time. The data was fitted to a power law of the form

$$\frac{D}{D_0} = \left(\frac{t_c - t}{t_c}\right)^{\alpha}$$

where D is the void diameter, D_0 is the initial void diameter, t_c is the full-collapse time, and α is a power coefficient. This functional form is based on a continuum level description of the collapse of a bubble in a homogeneous media due to Rayleigh.[48] The resulting fit together with the calculated data points are presented in Figure 9. The fit quality is high, with an R^2 value of 0.976, indicating that the process agrees well with the assumed collapse mechanism. The full-collapse time is 1.4 ps, in excellent agreement with the value obtained from the simulations (1.45 ps). The exponential coefficient is determined to be $\alpha = 0.19$, which is approximately half the value for a classical Rayleigh collapse ($\alpha = 0.4$). The initial structure of the void is a sphere with an average diameter of 5 nm. This structure remains stable during the first ~0.6 ps which is the duration it takes the shock wave to arrive at the void surface. As the shock starts to compress the void, nanojets form and are ejected into the void. The void is compressed and sheared, and its diameter shrinks accordingly. The shrinkage of the void can be seen as an inertial process, much like the collapse of single bubble sonoluminescence in water.[49] This is evidenced by the steadily growing velocity of the inward collapsing void walls. An estimate of the collapse velocity can be obtained by differentiating the numerical fit of the collapse dynamics with respect to time. The following velocities for the initial ($t = 0.6$ ps), intermediate ($t = 1.0$ ps), and near-final ($t = 1.35$ ps) wall velocities were obtained: 1.0, 1.8, and 9.6 km/s, respectively. Since the impact speed is high enough, the void collapse falls in the hydrodynamic regime. Therefore, the Rayleigh formula could be used to calculate the void collapse time using the relation

$$\tau_c = 0.45D\sqrt{\frac{\rho}{\Delta P}}$$

where ρ is the mass density, ΔP is the pressure difference across the void surface, and D is the void diameter. Using the values of the nanovoid, one obtains the critical time for the collapse, t_c = 1.44 ps, in excellent agreement with the result obtained in the simulations (Figure 9). This is quite unexpected since Rayleigh's formula does not take into account effects of viscosity or surface tension of the nanovoid. Furthermore, the aforementioned formula was derived under the assumption that a bubble is embedded in a uniform fluid, which is clearly not the case when the shock impacts the nanovoid in ETN.

CONCLUSIONS

The current study employed reactive molecular dynamics simulations based on the ReaxFF force field in conjunction with the symmetric plate impact methodology to study the mechanochemical response of crystalline improvised explosives. ETN, which is the nitrated form of the popular artificial sweetener, erythritol, was used as an example. It was demonstrated for the first time that the presence of nanoscale voids (5 nm diameter spheres) are sufficient to induce dramatic effects on the shock propagation characteristics and enhancement of the chemical decomposition in ETN. The formation of supersonic molecular nanojets was observed inside the 5 nm diameter void that resulted in local heating and an enhanced chemical decomposition rate. Moreover, it is revealed that the rate of void collapse closely follows the Rayleigh equation for bubble collapse in a homogeneous medium. This further induces the shock wave to travel faster, which is evident from inspection of the calculated density map. This behavior is not seen in the case of a perfect single crystal ETN, where the propagation velocity of the shock front remains largely constant. Higher temperatures that operate in the defected system lead to enhanced rates of molecular decomposition which in turn promote the generation of larger amounts of intermediates and stable final products, such as H_2O and N_2, although without altering the nature of the decomposition sequence which remains the unimolecular $N-NO_2$ bond cleavage. The carbon source almost entirely transforms into CO_2, which agrees nicely with experimental evidence and the positive oxygen balance of ETN. Remarkably, the presence of the 5 nm void does affect both the initial response of the material and the long-time chemistry in the defect containing system. The observation of late chemistry, on time scales much longer than shock propagation in the computational cell, was possible with the plate impact methodology used in the present study. The present study sheds light on the decomposition mechanism and response to shock loading of ETN, and thus should greatly assist future experimental characterization of this emerging improvised explosive.

AUTHOR INFORMATION

Notes

The authors declare no competing financial interest.

ACKNOWLEDGMENTS

This material is based upon work partially supported by the U.S. Department of Homeland Security, Science and Technology Directorate, Office of University Programs, under Grant 2013-ST-061-ED0001. The views and conclusions contained in this document are those of the authors and should not be interpreted as necessarily representing the official policies, either expressed or implied, of the U.S. Department of Homeland Security.

REFERENCES

(1) Buonassisi, T.; Istratov, A. A.; Marcus, M. A.; Lai, B.; Cai, Z. H.; Heald, S. M.; Weber, E. R. Engineering Metal-Impurity Nanodefects for Low-Cost Solar Cells. *Nat. Mater.* **2005**, *4*, 676−679.

(2) Mistry, H.; Varela, A. S.; Kühl, S.; Strasser, P.; Cuenya, B. R. Nanostructured Electrocatalysts with Tunable Activity and Selectivity. *Nature Reviews Materials* **2016**, *1*, 16009.

(3) Mochalin, V. N.; Shenderova, O.; Ho, D.; Gogotsi, Y. The Properties and Applications of Nanodiamonds. *Nat. Nanotechnol.* **2012**, *7*, 11−23.

(4) Pichot, V.; Risse, B.; Schnell, F.; Mory, J.; Spitzer, D. Understanding Ultrafine Nanodiamond Formation Using Nanostructured Explosives. *Sci. Rep.* **2013**, *3*, 2159.

(5) Tai, K.; Dao, M.; Suresh, S.; Palazoglu, A.; Ortiz, C. Nanoscale Heterogeneity Promotes Energy Dissipation in Bone. *Nat. Mater.* **2007**, *6*, 454−462.

(6) Felts, J. R.; Oyer, A. J.; Hernández, S. C.; Whitener, K. E., Jr.; Robinson, J. T.; Walton, S. G.; Sheehan, P. E. Direct Mechanochemical Cleavage of Functional Groups from Graphene. *Nat. Commun.* **2015**, *6*, 6467.

DOI: 10.1021/acs.jpcc.6b11543
J. Phys. Chem. C 2016, 120, 28886−28893

(7) Seidel, C. A. M.; Kuhnemuth, R. Mechanochemistry: Molecules under Pressure. *Nat. Nanotechnol.* **2014**, *9*, 164−165.
(8) Treacy, M. M. J.; Ebbesen, T. W.; Gibson, J. M. Exceptionally High Young's Modulus Observed for Individual Carbon Nanotubes. *Nature* **1996**, *381*, 678−680.
(9) Matyas, R.; Lycka, A.; Jirasko, R.; Jakovy, Z.; Maixner, J.; Miskova, L.; Kunzel, M. Analytical Characterization of Erythritol Tetranitrate, an Improvised Explosive. *J. Forensic Sci.* **2016**, *61*, 759−764.
(10) Xue, X.; Wen, Y.; Zhang, C. Early Decay Mechanism of Shocked E-Cl-20: A Molecular Dynamics Simulation Study. *J. Phys. Chem. C* **2016**, *120*, 21169−21177.
(11) Wen, Y. S.; Xue, X. G.; Long, X. P.; Zhang, C. Y. Cluster Evolution at Early Stages of 1,3,5-Triamino-2,4,6-Trinitrobenzene under Various Heating Conditions: A Molecular Reactive Force Field Study. *J. Phys. Chem. A* **2016**, *120*, 3929−3937.
(12) Yanilkin, A. V.; Sergeev, O. V. Molecular Dynamics Simulation of the Burning Front Propagation in PETN. *J. Phys. Conf Ser.* **2014**, *500*, 172010.
(13) Manaa, M. R.; Reed, E. J.; Fried, L. E.; Goldman, N. Nitrogen-Rich Heterocycles as Reactivity Retardants in Shocked Insensitive Explosives. *J. Am. Chem. Soc.* **2009**, *131*, 5483−5487.
(14) Budzien, J.; Thompson, A. P.; Zybin, S. V. Reactive Molecular Dynamics Simulations of Shock through a Single Crystal of Pentaerythritol Tetranitrate. *J. Phys. Chem. B* **2009**, *113*, 13142−13151.
(15) Frey, R. B. *Cavity Collapse in Energetic Materials*; Technical Report BRL-TR-2748; Defense Technical Information Center; 1986.
(16) Apin, A. Y.; Bobolev, V. K. The Effect of the Physical Structure and the State of Aggregation on the Detonating Capacity of Explosives. *Zh. Fiz. Khim.* **1946**, *20*, 1367−1370.
(17) Hirosaki, Y.; Murata, K.; Kato, Y.; Itoh, S. Effect of Void Size on the Detonation Pressure of Emulsion Explosives. *AIP Conf. Proc.* **2001**, *620*, 930−933.
(18) Maienschein, J. L.; Urtiew, P. A.; Garcia, F.; Chandler, J. B. Effect of Microvoids on the Shock Initiation of Petn. *AIP Conf Proc.* **1997**, *429*, 711−714.
(19) Palmas, P.; Botzanowski, T.; Guerain, M.; Forzy, A.; Bruneton, E.; Delrio, G. Size Determination of Porosity Inclusions in an Organic Solid Material by H-1 Nmr Diffusion and Sem-Fib Experiments: The Tatb Case. *J. Phys. Chem. B* **2016**, *120*, 4152−4159.
(20) Bourne, N. K.; Field, J. E. Explosive Ignition by the Collapse of Cavities. *Proc. R. Soc. London, Ser. A* **1999**, *455*, 2411−2426.
(21) Hamate, Y. A Computational Study of Microstructure Effects on Shock Ignition Sensitivity of Pressed RDX. *AIP Conf. Proc.* **2007**, *955*, 923−926.
(22) An, Q.; Goddard, W. A.; Zybin, S. V.; Luo, S. N. Inhibition of Hotspot Formation in Polymer Bonded Explosives Using an Interface Matching Low Density Polymer Coating at the Polymer-Explosive Interface. *J. Phys. Chem. C* **2014**, *118*, 19918−19928.
(23) Dlott, D. D.; Fayer, M. D. Shocked Molecular-Solids - Vibrational up Pumping, Defect Hot Spot Formation, and the Onset of Chemistry. *J. Chem. Phys.* **1990**, *92*, 3798−3812.
(24) Eason, R. M.; Sewell, T. D. Molecular Dynamics Simulations of the Collapse of a Cylindrical Pore in the Energetic Material A-Rdx. *Journal of Dynamic Behavior of Materials* **2015**, *1*, 423−438.
(25) Furman, D.; Dubnikova, F.; van Duin, A. C. T.; Zeiri, Y.; Kosloff, R. Reactive Force Field for Liquid Hydrazoic Acid with Applications to Detonation Chemistry. *J. Phys. Chem. C* **2016**, *120*, 4744−4752.
(26) Furman, D.; Kosloff, R.; Dubnikova, F.; Zybin, S. V.; Goddard, W. A.; Rom, N.; Hirshberg, B.; Zeiri, Y. Decomposition of Condensed Phase Energetic Materials: Interplay between Uni- and Bimolecular Mechanisms. *J. Am. Chem. Soc.* **2014**, *136*, 4192−4200.
(27) Furman, D.; Kosloff, R.; Zeiri, Y. Mechanism of Intact Adsorbed Molecules Ejection Using High Intensity Laser Pulses. *J. Phys. Chem. C* **2016**, *120*, 11306−11312.
(28) Hu, Y. H.; Brenner, D. W.; Shi, Y. F. Detonation Initiation from Spontaneous Hotspots Formed During Cook-Off Observed in Molecular Dynamics Simulations. *J. Phys. Chem. C* **2011**, *115*, 2416−2422.
(29) Rom, N.; Hirshberg, B.; Zeiri, Y.; Furman, D.; Zybin, S. V.; Goddard, W. A.; Kosloff, R. First-Principles-Based Reaction Kinetics for Decomposition of Hot, Dense Liquid Tnt from Reaxff Multiscale Reactive Dynamics Simulations. *J. Phys. Chem. C* **2013**, *117*, 21043−21054.
(30) Shan, T.-R.; Wixom, R. R.; Thompson, A. P. Extended Asymmetric Hot Region Formation Due to Shockwave Interactions Following Void Collapse in Shocked High Explosive. *Phys. Rev. B: Condens. Matter Mater. Phys.* **2016**, *94*, 054308.
(31) Willey, T. M.; Hoffman, D. M.; van Buuren, T.; Lauderbach, L.; Gee, R. H.; Maiti, A.; Overturf, G. E.; Fried, L. E.; Ilavsky, J. The Microstructure of Tatb-Based Explosive Formulations During Temperature Cycling Using Ultra-Small-Angle X-Ray Scattering. *Propellants, Explos., Pyrotech.* **2009**, *34*, 406−414.
(32) Willey, T. M.; van Buuren, T.; Lee, J. R. I.; Overturf, G. E.; Kinney, J. H.; Handly, J.; Weeks, B. L.; Ilavsky, J. Changes in Pore Size Distribution Upon Thermal Cycling of Tatb-Based Explosives Measured by Ultra-Small Angle X-Ray Scattering. *Propellants, Explos., Pyrotech.* **2006**, *31*, 466−471.
(33) Nomura, K. I.; Kalia, R. K.; Nakano, A.; Vashishta, P. Reactive Nanojets: Nanostructure-Enhanced Chemical Reactions in a Defected Energetic Crystal. *Appl. Phys. Lett.* **2007**, *91*, 183109.
(34) Zhou, T.; Lou, J.; Zhang, Y.; Song, H.; Huang, F. Hot Spot Formation and Chemical Reaction Initiation in Shocked Hmx Crystals with Nanovoids: A Large-Scale Reactive Molecular Dynamics Study. *Phys. Chem. Chem. Phys.* **2016**, *18*, 17627−17645.
(35) Zhao, S.; Germann, T. C.; Strachan, A. Molecular Dynamics Simulation of Dynamical Response of Perfect and Porous Ni/Al Nanolaminates under Shock Loading. *Phys. Rev. B: Condens. Matter Mater. Phys.* **2007**, *76*, 014103.
(36) Zhao, S. J.; Germann, T. C.; Strachan, A. Atomistic Simulations of Shock-Induced Alloying Reactions in Ni/Al Nanolaminates. *J. Chem. Phys.* **2006**, *125*, 164707.
(37) Loboiko, B. G.; Lubyatinsky, S. N. Reaction Zones of Detonating Solid Explosives. *Combust., Explos. Shock Waves* **2000**, *36*, 716−733.
(38) Shan, T. R.; Thompson, A. P. Shock-Induced Hotspot Formation and Chemical Reaction Initiation in PETN Containing a Spherical Void. *J. Phys. Conf Ser.* **2014**, *500*, 172009.
(39) Holian, B. L. Modeling Shock-Wave Deformation Via Molecular-Dynamics. *Phys. Rev. A: At., Mol., Opt. Phys.* **1988**, *37*, 2562−2568.
(40) Ranjan, D.; Oakley, J.; Bonazza, R. Shock-Bubble Interactions. *Annu. Rev. Fluid Mech.* **2011**, *43*, 117−140.
(41) Holyst, R.; Litniewski, M.; Garstecki, P. Large-Scale Molecular Dynamics Verification of the Rayleigh-Plesset Approximation for Collapse of Nanobubbles. *Phys. Rev. E* **2010**, *82*, 066309.
(42) Oxley, J. C.; Smith, J. L.; Brady, J. E.; Brown, A. C. Characterization and Analysis of Tetranitrate Esters. *Propellants, Explos., Pyrotech.* **2012**, *37*, 24−39.
(43) Manner, V. W.; Preston, D. N.; Tappan, B. C.; Sanders, V. E.; Brown, G. W.; Hartline, E.; Jensen, B. Explosive Performance Properties of Erythritol Tetranitrate (Etn). *Propellants, Explos., Pyrotech.* **2015**, *40*, 460−462.
(44) Ng, W. L.; Field, J. E.; Hauser, H. M. Study of the Thermal Decomposition of Pentaerythritol Tetranitrate. *J. Chem. Soc., Perkin Trans. 2* **1976**, 637−639.
(45) Ng, W. L.; Field, J. E.; Hauser, H. M. Thermal, Fracture, and Laser-Induced Decomposition of Pentaerythritol Tetranitrate. *J. Appl. Phys.* **1986**, *59*, 3945−3952.
(46) Levesque, G.; Vitello, P.; Howard, W. M. Hot-Spot Contributions in Shocked High Explosives from Mesoscale Ignition Models. *J. Appl. Phys.* **2013**, *113*, 233513.
(47) Fu, H. H.; Comer, J.; Cai, W. S.; Chipot, C. Sonoporation at Small and Large Length Scales: Effect of Cavitation Bubble Collapse on Membranes. *J. Phys. Chem. Lett.* **2015**, *6*, 413−418.

DOI: 10.1021/acs.jpcc.6b11543
J. Phys. Chem. C 2016, 120, 28886−28893

(48) Brennen, C. E. *Cavitation and Bubble Dynamics*; Cambridge University Press: 2013.
(49) Plesset, M. S.; Prosperetti, A. Bubble Dynamics and Cavitation. *Annu. Rev. Fluid Mech.* **1977**, *9*, 145−85.

DOI: 10.1021/acs.jpcc.6b11543
J. Phys. Chem. C 2016, 120, 28886−28893